

Minimal model for low-energy electronic states of twisted bilayer graphene

Stephen Carr,¹ Shiang Fang,¹ Ziyang Zhu,¹ and Efthimios Kaxiras^{1,2}

¹*Department of Physics, Harvard University, Cambridge, Massachusetts 02138, USA*

²*John A. Paulson School of Engineering and Applied Sciences, Harvard University, Cambridge, Massachusetts 02138, USA*

We introduce a physically motivated minimal model for the electronic structure of twisted bilayer graphene (tBLG), which incorporates the crucial role of lattice relaxation. Our model, based on $k \cdot p$ perturbation theory, combines the accuracy of DFT calculations through effective tight-binding Hamiltonians with the computational efficiency and complete control of the twist angle offered by continuum models. The inclusion of relaxation significantly changes the bandstructure at the first magic-angle twist corresponding to flat bands near the Fermi level (the “low-energy” states), and eliminates the appearance of a second magic-angle twist. We argue that the minimal model for the low-energy states of tBLG consists of ten bands, necessary to capture the changes in electronic states as a function of twist angle. We also provide information on the nature of these bands through their wavefunctions, which is closely tied to the features of the atomic relaxation.

The discovery of correlated phases in twisted bilayer graphene (tBLG) has generated much interest in this structurally and compositionally rather simple system; it has emerged as a new platform for tunable electronic correlations, and for exploring of the nature of unconventional superconductivity^{1,2}. The challenge in modeling these phenomena from an atomistic perspective is that the actual structure of tBLG near the magic-angle twist ($\sim 1.1^\circ$) where correlated behavior is observed, consists of a large number of atoms, exceeding 10^4 . To make progress from the theoretical point of view, a minimal model is needed that can capture the essence of single-particle states near the Fermi level (“low-energy” states). Such a model should reproduce the energy spectrum as a function of their relative twist angle with reasonable accuracy and with the required fidelity in capturing the *nature* of low-energy states. The appearance of correlated behavior is related to bands with very low dispersion (“flat” bands) caused by interlayer hybridization between the two Dirac cones from the different layers³⁻⁶.

Existing models based on DFT calculations^{7,8} or large supercell tight-binding Hamiltonians⁹⁻¹¹ are too complex to form the basis of a realistic many-body theory. At the other extreme, simplified continuum models allow for efficient calculations, but are based on heuristic arguments about the nature of the relevant electronic states¹²⁻¹⁵. An important feature of the physical system is the presence of atomic relaxation near the magic-angle twist, which has significant effects on the low-energy bandstructure^{10,16-19}. Many simplified models for the flat bands of magic-angle tBLG have been proposed based on symmetry analysis, but they rely on empirical parameterization and are designed for only the magic-angle twist configuration²⁰⁻²², typically ignoring atomic relaxation. Here, we present an *ab initio* $k \cdot p$ perturbation continuum model for tBLG which accurately accounts for the effects of atomic relaxation. Our model reproduces the results of DFT-quality tight-binding Hamiltonians but at a smaller computational cost and, more importantly, it applies to all twist angles near the magic-angle value. Using this model, we draw conclusions on

the behavior of correlated states at small twist angles, including the interesting result that there are no flat bands in the range of the expected second magic-angle twist ($\sim 0.5^\circ$). For reference, we compare our continuum model to the seminal and widely employed $k \cdot p$ model of Bitztritter and MacDonald¹³ (BMD in the following), and we adopt their dimensionless parameter $\alpha = \omega/v_F k_\theta$ for describing the twist-angle θ , where v_F is the Fermi velocity, k_θ is the wave-vector set by the moiré length scale and ω is the effective interlayer coupling strength.

Within $k \cdot p$ perturbation theory, the set of Bloch states of the two graphene layers is augmented by the addition of interlayer couplings due to the twist-angle induced Umklapp scattering process. As the low-energy electronic structure of tBLG is dominated by a pair of Dirac cones, the momentum expansion can be carried out about one copy of the cone at a valley K point. Taking also into account spin degeneracy, each band represents four electronic states in a real system²³. Here we introduce an expanded *ab initio* $k \cdot p$ model which gives a more complete physical picture of the tBLG system. Our model has three new key ingredients:

- (1) relaxation of the bilayer system²⁴, including the out-of-plane relaxation of different regions as well as the in-plane strain corrections to the Hamiltonian of the individual monolayers;
- (2) terms beyond the first shell of couplings in the $k \cdot p$ continuum model, which are necessary to capture the changes in stacking order at small angles;
- (3) inclusion of k -dependent terms, which allow the $k \cdot p$ model to reproduce more accurately the particle-hole asymmetry of realistic *ab initio* bandstructures.

The $k \cdot p$ terms are directly computed from an *ab initio* tight-binding Hamiltonian model²⁵⁻²⁷ for supercells spanning the twist-angle range $0.18^\circ \leq \theta \leq 6^\circ$. These terms have smooth dependence on θ , allowing for interpolation between the specific twist angles that correspond to finite supercells, to generate a model valid for any desired angle in that range. We relegate the detailed description of the extended Hamiltonian and the procedure for obtaining the relevant terms of the continuum model

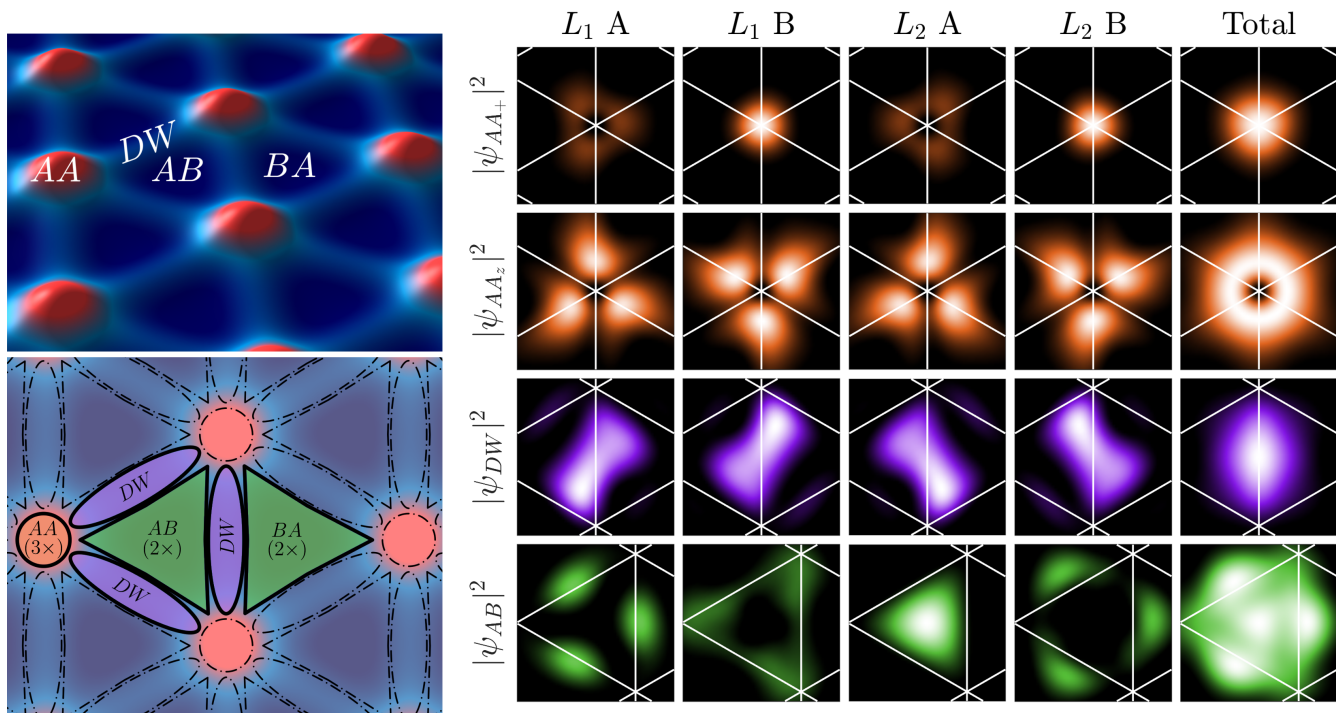


FIG. 1. Left: Structure of relaxed tBLG at $\theta = 0.9^\circ$ with exaggerated vertical relaxation (top). AA, AB and BA stackings, and domain walls (DW) are labeled along with a schematic representation (bottom) of the 10 orbitals per unit cell of the moiré pattern required to describe the low-energy electronic states: 3 at the AA region, 1 at each of the 3 DW regions, and 2 at each of the AB and BA regions. Right: Wavefunction magnitudes, $|\psi_l|^2$, $l = AA_z, AA_\pm, DW, AB/BA$, of the 10-band model, at $\theta = 0.9^\circ$, projected in the two layers (L_1 and L_2) and the sublattices A and B of each layer; the total (far-right column) is the sum of all layer and sublattice contributions (see SM for additional discussion). The underlying moiré supercell lattice is given by the thin white lines.

to a companion paper²⁸.

Our continuum model affords a natural interpretation of the electronic structure of tBLG at small twist angles, which is derived directly from the atomic relaxation so we describe this aspect first. For twist-angle θ smaller than a critical value $\theta_c \approx 1^\circ$, the local atomic structure near the AA and AB stackings of the two layers becomes *independent* of θ . This creates a pattern of small circular domains of AA stacking and large triangular domains of AB/BA stackings. Domain walls (DW) of intermediate stacking separate the AB and BA domains and connect the AA regions. This creates local electronic environments which are locked-in with respect to changing twist-angle for $\theta < \theta_c$, where the tBLG system consists of a few fixed elements^{10,18,24}, and only their length scale changes for decreasing twist angle. These elements are: the AA regions which have a *local* twist of $\theta_{AA} = 1.7^\circ$, which is *independent* of the overall twist angle θ between the two layers, the AB and BA regions with negligible local twist. Moreover, the diameter of the AA regions and the width of the DW regions are approximately equal and remain unchanged for $\theta < \theta_c$ ¹⁸. These features are shown in Fig. 1 for $\theta = 0.9^\circ$.

The relaxation in tBLG is described by two simultaneous effects. In-plane relaxation decreases the area of

the high stacking energy AA region while it increases that of low stacking energy AB/BA regions. Out-of-plane relaxation causes corrugation, increasing the vertical separation between the AA regions from the equilibrium distance in AB stacking of 3.35 Å to 3.59 Å, a substantial change ($> 7\%$). The reduction in the size of AA stacking can be understood as a minimization of planar stress energy and stacking energies, and has been modeled through various methods^{10,17,18,24} leading to a relaxed pattern in agreement with experimental results^{16,29}. The role of vertical relaxation in experimental devices is less understood, as only free-standing tBLG has been modeled. Experimental tBLG devices are typically encapsulated in hexagonal Boron Nitride, so the actual corrugation may be reduced compared to the free-standing case. To take this into account, we consider two limits of the vertical relaxation: a “Full” relaxation model (free-standing bilayer result) and a “Flat” model with constant interlayer distance equal to the average of AA and AB interlayer distances (3.47 Å). The magic angle predicted by the fully relaxed model, $\theta_c \approx 1.0^\circ$, is closer to the experimentally observed value $\theta_c^{\text{exp}} \approx 1.08^\circ$.

The low-energy electronic states are directly associated with and derive from the presence of the relaxation-induced structural elements described earlier. A minimal

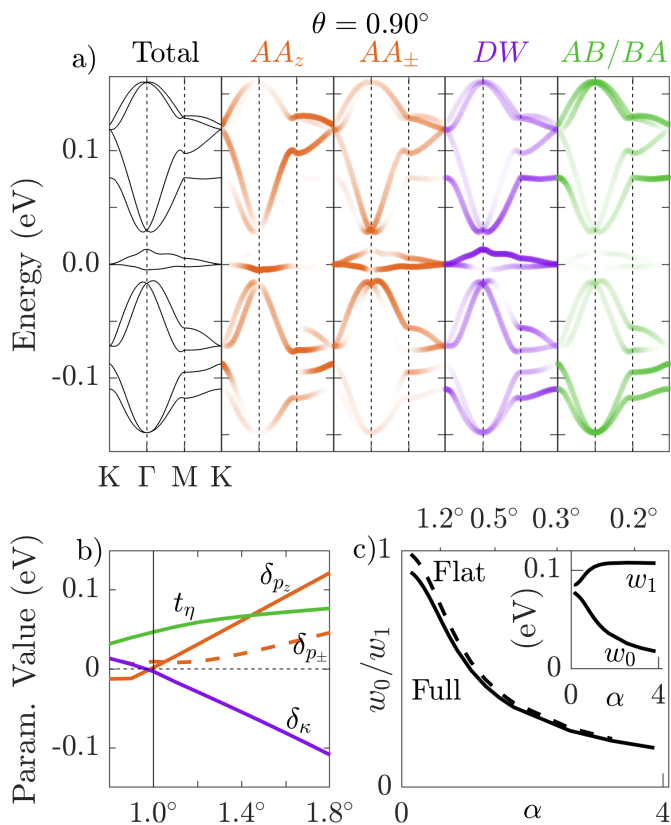


FIG. 2. (a) Orbital character of the bands in the reduced 10-band $k \cdot p$ model at $\theta = 0.90^\circ < \theta_c$. (b) Schematic representation of the different terms in the Hamiltonian in the reduced model: $\delta_{p_z}, \delta_{p_\pm}$ are the chemical potentials of the AA_z, AA_\pm orbitals, δ_κ is the chemical potential of the DW and t_η is the nearest-neighbor coupling between AB/BA orbitals. (c) Dependence of the interlayer $k \cdot p$ coupling terms on the twist angle θ from 6° to 0.18° . The inset gives the value of the individual terms with full relaxation, and the main panel gives their ratio for both flat and full relaxation.

model that can adequately capture all the essential features of the low-energy states consists of 10 bands; a similar model has been introduced on the basis of symmetry arguments²⁰. This model comprises three orbitals on a triangular lattice formed by the AA sites, one of p_z -like character (AA_z) and two of $(p_x \pm ip_y)$ -like character (AA_\pm), three orbitals on a Kagome lattice formed by the domain walls, and four orbitals on a honeycomb lattice, two for each of the AB and BA domains. Each of the orbitals form sublattice Hamiltonians (H^l) with independent on-site energies μ^l and hopping terms t^l and have independent effective chemical potentials δ_l expressed in terms of μ^l and t^x ,

$$H^l = \mu^l \sum_{i=1}^{n_l} c_i^\dagger c_i + \sum_{i,j=1}^{n_l} t_{ij}^l c_i^\dagger c_j, \quad \delta_l \equiv \mu^l + m_l t^l$$

with indices i, j running over the orbitals in each sublattice, $l = AA_z, AA_\pm, DW, AB/BA$, and $n_l = 1, 2, 3$ and $m_l = 6, -3, 4$ for $l = AA_z, AA_\pm$ and DW respectively. The sublattice Hamiltonians are also coupled to one another through inter-orbital hoppings (C_1, \dots, C_5) so the full Hamiltonian is given by (for a complete description see SM):

$$H = \begin{pmatrix} H^{AA_z} & C_1^\dagger & 0 & C_2^\dagger \\ C_1 & H^{AA_\pm} & C_3^\dagger & C_4^\dagger \\ 0 & C_3 & H^{DW} & C_5^\dagger \\ C_2 & C_4 & C_5 & H^{AB/BA} \end{pmatrix}$$

To compare our *ab initio* $k \cdot p$ results to this model, we project non-orthogonal wavefunctions that satisfy the symmetry conditions, shown in Fig. 1, from band structure calculations. We fit the model parameters for $\theta \in [0.8^\circ, 1.8^\circ]$, to reproduce the *ab initio* bands (see SM). In Fig. 2c, the δ_l for the AA and DW type orbitals reach the critical behavior $\delta_l = 0$ only at the magic angle value $\theta_c \approx 1.0^\circ$. The flat bands near the magic angle have AA and DW character (see Fig. 2a), showing that the coupling between these states is a necessary ingredient of the model if it is to capture the electronic structure as a function of twist angle. In particular, the orbital character of the electron and hole bands flips at the magic-angle twist: the hole band has DW character for $\theta > \theta_c$ and switches to AA_z character for $\theta < \theta_c$, while the electron band has the reverse character. We emphasize that the form of these wavefunctions is not sensitive to the twist-angle, and is robust for twist angles within $\pm 0.2^\circ$ of the magic angle.

Two other important parameters in the $k \cdot p$ model are the effective interlayer coupling between orbitals of the same sublattice label, $A \rightarrow A$ or $B \rightarrow B$, and that between orbitals of different labels, $A \rightarrow B$ or $B \rightarrow A$. These nearest-neighbor interlayer couplings have been labeled $w_i, i = 0, 1$ in previous studies and have a simple geometric interpretation: w_0 is the interlayer electronic coupling at the AA sites and w_1 is the coupling at AB/BA sites, averaged over the entire moiré cell. The values of these w_i parameters depend strongly on the twist angle θ . As the lattice relaxes, the relative size of the AA regions is greatly reduced while that of the AB/BA regions is increased, causing a reduction in the value of w_0 and a modest increase in the value of w_1 . This dependence is shown in Fig. 2c for the Full and the Flat relaxation models. The overall θ dependence of the ratio w_0/w_1 is not sensitive to the relaxed height assumption. The Flat model has a larger ratio as the Full relaxation assumption moves the AB/BA sites closer together (increasing their coupling and the w_1 value) while moving the AA sites farther apart (reducing their coupling and the w_0 value).

To elucidate the salient features of the single-particle model, we study three related indicators of the flat-band phenomenon as a function of θ : the Fermi velocity (v_F), the bandwidth (E_w), and the band gap (E_g). These

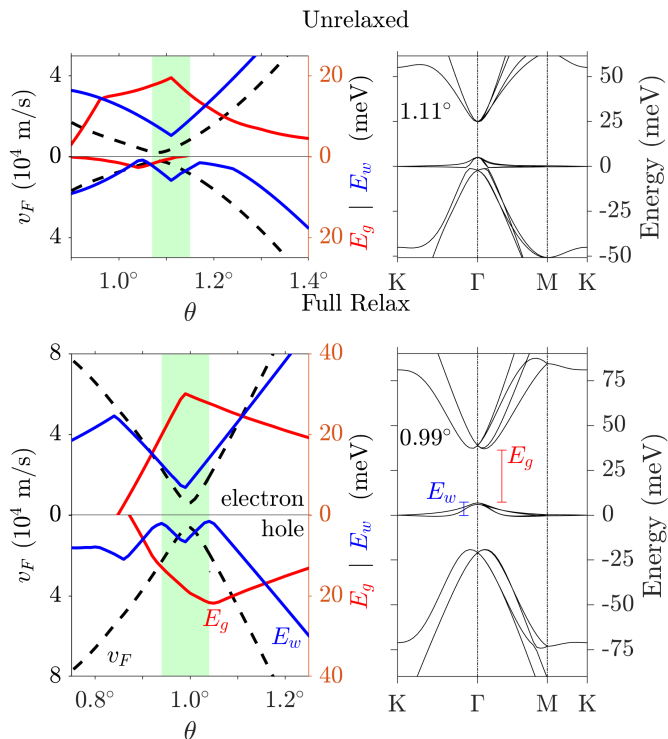


FIG. 3. Left panels: Features of the flat bands near the magic-angle for models with or without atomic relaxation: the Fermi velocity v_F (dashed black line, left axis), band gap E_g (red lines, right axis), and bandwidth E_w (blue lines, right axis) for the electron and hole states. In-plane relaxation creates a more well defined magic angle regime (green shaded region) in all three features. Right panels: corresponding bandstructures in the magic-angle regime.

are shown in Fig 3. All three are calculated for both the electron and the hole sides of the flat-band manifold. The model *without* relaxation shows large discrepancies between the extrema of the Fermi velocity, gap, and bandwidth, and the electron and hole features have little in common. The two models (Flat and Full) that include relaxation show more regular dependence on θ and closer correspondence between the electron and hole bands. The bandwidth for the hole band is always smaller than that of the electron band, and the hole band achieves its minimum twice. In general, $v_F = 0$ does not coincide with bandwidth minima. We thus draw the important conclusion that *the magic-angle is not a single value, but rather a range of $\approx 0.1^\circ$ which spans the extrema in these key features*. This range for the Full relaxed model is $\theta \in [0.95^\circ, 1.05^\circ]$ and $\theta \in [0.80^\circ, 0.90^\circ]$ for the Flat model. The bandstructures for both models are indistinguishable but occur at different twist-angle values, shifted by 0.15° (the critical value is smaller for the Flat model).

An interesting behavior of the Full relaxed model occurs at the center of the magic-angle regime: although the Dirac cone still has symmetric dispersion near the

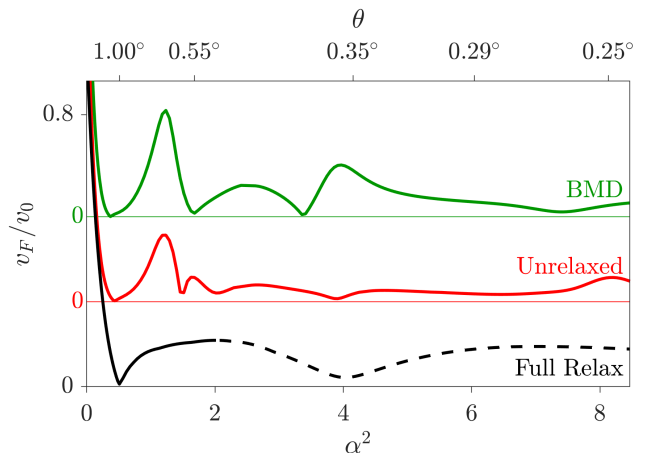


FIG. 4. Normalized Fermi velocity as a function of $\alpha^2 \propto 1/\theta^2$ for the BMD and the *ab initio* $k \cdot p$ models without relaxation (Unrelaxed) and with atomic relaxation (Full relaxed). Relaxed calculations below $\theta = 0.5^\circ$ have not been validated against tight-binding results, shown as a dashed line.

K-point, the hole band dispersion is such that near the Γ point its energy is *higher* than the Fermi level. Thus the charge neutrality point does *not* occur at the Dirac point energy. This effect persists in all of the *ab initio* $k \cdot p$ models (even without relaxation), and is a behavior that can be observed in other tight-binding models in the literature^{10,11} but was not explicitly pointed out before. For transport measurement, this behavior would result in a range of 0.1° in twist angle where the charge neutrality point of the flat bands does not align with the resistive Dirac-point feature, as well as a reduction in the overall resistivity at the Dirac-point energy.

Another important result of our calculations including atomic relaxation in tBLG is the suppression of the second magic-angle twist, defined as a smaller twist angle at which $v_F = 0$ ¹³. In Fig. 4 we show the Fermi velocity as predicted from the BMD model and from our unrelaxed and fully relaxed *ab initio* $k \cdot p$ models. Although our unrelaxed model shows similar behavior to the BMD model with a second magic angle occurring near $\theta = 0.5^\circ$, the inclusion of atomic relaxation removes this feature in near 0.5° . In both the BMD and unrelaxed models, the second magic angle near 0.5° is only defined by $v_F = 0$, but there are no extrema in the bandwidth or bandgap at this angle. This can be understood from a careful study of how the ratio w_0/w_1 affects the stability of the flat-band feature³⁰. The Full relaxed model shows a possible dip in the Fermi velocity, corresponding to a possible second magic angle, near $\alpha \approx 2$ or $\theta = 0.35^\circ$. However our model needs further refinement to make accurate predictions for very small θ , as our current model includes terms only up to the third shell in momentum space. We are not certain this dip in v_F will persist when additional terms are included. The lattice relaxation in tBLG becomes increasingly sharp on the moiré length scale as the twist angle decreases^{10,16–18,24}, and sharper

features in the relaxation introduce additional important couplings in the $k \cdot p$ model at larger momenta.

ACKNOWLEDGMENTS

We thank Daniel Massatt, Hoi Chun Po, Alex Kruchkov, Grigory Tarnopolskiy, Pablo Jarillo-Herrero,

Hyobin Yoo, Rebecca Engelke, and Philip Kim for useful discussions. This work was supported by ARO MURI Award W911NF-14-0247 and by the STC Center for Integrated Quantum Materials, NSF Grant No. DMR-1231319. The computations in this paper were run on the Odyssey cluster supported by the FAS Division of Science, Research Computing Group at Harvard University.

-
- ¹ Y. Cao, V. Fatemi, A. Demir, S. Fang, S. L. Tomarken, J. Y. Luo, J. D. Sanchez-Yamagishi, K. Watanabe, T. Taniguchi, E. Kaxiras, R. C. Ashoori, and P. Jarillo-Herrero, *Nature* **556**, 80 EP (2018).
- ² Y. Cao, V. Fatemi, S. Fang, K. Watanabe, T. Taniguchi, E. Kaxiras, and P. Jarillo-Herrero, *Nature* **556**, 43 EP (2018).
- ³ G. Li, A. Luican, J. M. B. Lopes dos Santos, A. H. Castro Neto, A. Reina, J. Kong, and E. Y. Andrei, *Nature Physics* **6**, 109 (2009).
- ⁴ I. Brihuega, P. Mallet, H. González-Herrero, G. Trambly de Laissardière, M. M. Ugeda, L. Magaud, J. M. Gómez-Rodríguez, F. Ynduráin, and J.-Y. Veuillen, *Physical review letters* **109**, 196802 (2012).
- ⁵ A. Luican, G. Li, A. Reina, J. Kong, R. R. Nair, K. S. Novoselov, A. K. Geim, and E. Y. Andrei, *Phys. Rev. Lett.* **106**, 126802 (2011).
- ⁶ D. Wong, Y. Wang, J. Jung, S. Pezzini, A. M. DaSilva, H.-Z. Tsai, H. S. Jung, R. Khajeh, Y. Kim, J. Lee, S. Kahn, S. Tollabimazraehno, H. Rasool, K. Watanabe, T. Taniguchi, A. Zettl, S. Adam, A. H. MacDonald, and M. F. Crommie, *Physical Review B* **92**, 155409 (2015).
- ⁷ G. Trambly de Laissardière, D. Mayou, and L. Magaud, *Nano Letters* **10**, 804 (2010), pMID: 20121163, <https://doi.org/10.1021/nl902948m>.
- ⁸ K. Uchida, S. Furuya, J.-I. Iwata, and A. Oshiyama, *Physical Review B* **90**, 155451 (2014).
- ⁹ E. Suárez Morell, J. D. Correa, P. Vargas, M. Pacheco, and Z. Barticevic, *Phys. Rev. B* **82**, 121407 (2010).
- ¹⁰ N. N. T. Nam and M. Koshino, *Phys. Rev. B* **96**, 075311 (2017).
- ¹¹ M. Angeli, D. Mandelli, A. Valli, A. Amaricci, M. Capone, E. Tosatti, and M. Fabrizio, *arXiv:1809.11140 [cond-mat.str-el]* (2018).
- ¹² E. J. Mele, *Phys. Rev. B* **81**, 161405 (2010).
- ¹³ R. Bistritzer and A. H. MacDonald, *Proceedings of the National Academy of Sciences of the United States of America* **108**, 12233 (2011).
- ¹⁴ P. San-Jose, J. González, and F. Guinea, *Physical review letters* **108**, 216802 (2012).
- ¹⁵ D. Weckbecker, S. Shallcross, M. Fleischmann, N. Ray, S. Sharma, and O. Pankratov, *Phys. Rev. B* **93**, 035452 (2016).
- ¹⁶ H. Yoo, K. Zhang, R. Engelke, S. Carr, S. Fang, P. Cazeaux, S. H. Sung, R. Hovden, A. W. Tsien, T. Taniguchi, K. Watanabe, G.-C. Yi, M. Kim, M. Lusk, E. B. Tadmor, E. Kaxiras, and P. Kim, *arXiv:1804.03806 [cond-mat.mtrl-sci]* (2018).
- ¹⁷ S. Dai, Y. Xiang, and D. J. Srolovitz, *Nano Letters* **16**, 5923 (2016), pMID: 27533089, <http://dx.doi.org/10.1021/acs.nanolett.6b02870>.
- ¹⁸ K. Zhang and E. B. Tadmor, *Journal of the Mechanics and Physics of Solids* **112**, 225 (2018).
- ¹⁹ X. Lin, D. Liu, and D. Tomnek, *arXiv:1811.00413 [cond-mat.mes-hall]* (2018).
- ²⁰ H. C. Po, L. Zou, T. Senthil, and A. Vishwanath, *arXiv:1808.02482 [cond-mat.str-el]* (2018).
- ²¹ N. F. Q. Yuan and L. Fu, *Phys. Rev. B* **98**, 045103 (2018).
- ²² M. Koshino, N. F. Q. Yuan, T. Koretsune, M. Ochi, K. Kuroki, and L. Fu, *Phys. Rev. X* **8**, 031087 (2018).
- ²³ Here we consider only a single (monolayer) valley, but the contribution of the second valley can be included by sampling the C_2 transformation of the original path in momentum space. The two valleys give slightly different bandstructures along the Γ to M line but are identical along other high-symmetry lines.
- ²⁴ S. Carr, D. Massatt, S. B. Torrisi, P. Cazeaux, M. Lusk, and E. Kaxiras, *arXiv:1805.06972 [cond-mat.mes-hall]* (2018).
- ²⁵ S. Fang and E. Kaxiras, *Physical Review B* **93**, 235153 (2016).
- ²⁶ S. Fang, S. Carr, M. A. Cazalilla, and E. Kaxiras, *Phys. Rev. B* **98**, 075106 (2018).
- ²⁷ S. Carr, S. Fang, P. Jarillo-Herrero, and E. Kaxiras, *Phys. Rev. B* **98**, 085144 (2018).
- ²⁸ in preparation.
- ²⁹ J. S. Alden, A. W. Tsien, P. Y. Huang, R. Hovden, L. Brown, J. Park, D. A. Muller, and P. L. McEuen, *Proceedings of the National Academy of Sciences* **110**, 11256 (2013), <http://www.pnas.org/content/110/28/11256.full.pdf>.
- ³⁰ G. Tarnopolsky, A. J. Kruchkov, and A. Vishwanath, *arXiv:1808.05250 [cond-mat.str-el]* (2018).

**Supplementary Material: Minimal model for low-energy
electronic states of twisted bilayer graphene**

Stephen Carr,¹ Shiang Fang,¹ Ziyang Zhu,¹ and Efthimios Kaxiras^{1,2}

*¹Department of Physics, Harvard University,
Cambridge, Massachusetts 02138, USA*

*²John A. Paulson School of Engineering and Applied Sciences,
Harvard University, Cambridge, Massachusetts 02138, USA*

arXiv:1901.03420v2 [cond-mat.mes-hall] 30 Jan 2019

I. RELAXATION OF TWISTED BILAYER GRAPHENE

The rigid twisted bilayer is subject to the atomic relaxations to minimize the total energy of the crystal. Here we assume D_6 rotational symmetry at an AA stacking site (e.g. the rotation axis is through the center of a hexagon, not a Carbon site). Regions with different local atomic registry differ in their stacking energy. We use a generalized stacking fault energy (GSFE) functional from DFT calculations¹ to capture this registry-dependent energy. The conventional AB/BA (Bernal) stacking are of lowest energy, and so relaxed domains of locally AB/BA stacking are favored in the twisted bilayer graphene crystal at angles below 2° . Regions of AA stacking spots are reduced with domain boundary line formation in between neighboring AB/BA regions. Another feature is the puckered out-of-plane crystal relaxations. The vertical layer separation is shortest (longest) for the locally AB/BA (AA) stacking region. The above qualitative description of the relaxed twisted bilayer graphene crystal is substantiated by *ab initio* calculations and continuum models, and for further details we refer to Ref. 2.

The structural deformation can be described by an in-plane shift vector $\mathbf{u}^i(\mathbf{r}) = (u_x^i(\mathbf{r}), u_y^i(\mathbf{r}))$ and an out-of-plane component $h^i(\mathbf{r})$. This causes lattice relaxation by mapping unrelaxed positions \mathbf{r} in the i -th layer of the rigid bilayer to $\mathbf{r} + \mathbf{u}^i(\mathbf{r}) + h^i(\mathbf{r})\hat{z}$. The relaxation pattern respects the three-fold rotation symmetry and mirror symmetry of the bilayer, and the functional form can be Fourier expanded:

$$\mathbf{u}^i(\mathbf{r}) = -i \sum_{\mathbf{q}} u_{\mathbf{q}}^i e^{i\mathbf{q}\cdot\mathbf{r}}, h^i(\mathbf{r}) = h_0 + \sum_{\mathbf{q}} h_{\mathbf{q}} e^{i\mathbf{q}\cdot\mathbf{r}} \quad (1)$$

Symmetry requires $u_{\mathbf{q}'}^1 = R_{60^\circ} u_{\mathbf{q}}^1$ and $h_{\mathbf{q}'} = h_{\mathbf{q}}$ when \mathbf{q}' is 60° rotated from \mathbf{q} and R_{60° the 60° rotation matrix for the vector. The \mathbf{q} 's are sums of the reciprocal lattice parameters, $\mathbf{q} = m\mathbf{G}_1 + n\mathbf{G}_2$ for integers m, n and reciprocal lattice vectors G_i . In practice, we use up to $m, n = 20$ to model the relaxation accurately down to $\theta = 0.18^\circ$, but for $\theta \geq 1^\circ$ only the first two ($m, n = 2$) components are usually needed.

II. CONTINUUM HAMILTONIAN FOR RELAXED TBLG

Our low-energy effective $k \cdot p$ Hamiltonian for relaxed twisted bilayer graphene (tBLG) has the following form:

$$\tilde{H}_K = \begin{bmatrix} H_D^1(\mathbf{k}) + A_1(\mathbf{r}) + V_1(\mathbf{r}) & \tilde{T}^\dagger(\mathbf{r}) + \{M_+^\dagger(\mathbf{r}), \hat{k}_-\} + \{M_-^\dagger(\mathbf{r}), \hat{k}_+\} \\ \tilde{T}(\mathbf{r}) + \{M_+(\mathbf{r}), \hat{k}_+\} + \{M_-(\mathbf{r}), \hat{k}_-\} & H_D^2(\mathbf{k}) + A_2(\mathbf{r}) + V_2(\mathbf{r}) \end{bmatrix} \quad (2)$$

- $H_D^i(\mathbf{k})$ is the Dirac Hamiltonian for each individual graphene monolayer layer.
- $V_i(\mathbf{r})$ terms are the external potential we can introduce to each layer. These could include the electric gating potential, sublattice mass terms and the modulated electric potential from doping and charge redistribution.
- $A_i(\mathbf{r})$ is the in-plane pseudo-gauge field coupled to the Dirac electron. These terms are generated from the geometric deformation and strain for each layer. When expanded in Fourier components with supercell reciprocal lattice vectors, it can be written as $A_i(\mathbf{r}) = \sum_{\mathbf{p}_i} A_{\mathbf{p}_i}^i e^{i\mathbf{p}_i \cdot \mathbf{r}}$.
- The first part of the inter-layer coupling term $\tilde{T}(\mathbf{r})$ gives the scattering terms as in the original BMD model³. However, we generalize the expansion to include higher-order terms as $\tilde{T}(\mathbf{r}) = \sum_{\mathbf{q}_i} \tilde{T}_{\mathbf{q}_i} e^{i\mathbf{q}_i \cdot \mathbf{r}}$.
- The remaining part of the inter-layer coupling terms, with $\hat{k}_\pm = \hat{k}_x \pm i\hat{k}_y$, are the momentum dependent scattering terms. They are relevant for the particle-hole asymmetric features of the tight-binding band structures. The anti-commutator notation is used to symmetrize the non-commuting operators \hat{r} and \hat{k} .
- The coupling constants here are investigated numerically with twist angle dependence. They are derived from the projection of supercell calculations with relaxed geometry obtained from elastic theory.

III. VALIDATION OF BAND STRUCTURES

Here we compare of bandstructures of our full tight-binding model, our $k \cdot p$ model, and the reduced 10-band model⁴ across four representative angles. The $k \cdot p$ model perfectly recreates the low-energy tight-binding band structures if we sample over both valleys of the monolayers (their bands only differ here on the Γ to M line). The 10-band model for each angle is obtained by first computing the $k \cdot p$ model, and then optimizing the 10-band model's 18 parameters to minimize

$$\text{Err} = \sum_{b=1}^{10} w_b \sqrt{\sum_{\mathbf{k}} (E_b(\mathbf{k}) - \epsilon_b(\mathbf{k}))^2}$$

where E_b are the eigenvalues of the 10-band model for band b and ϵ_b are the pre-computed eigenvalues for the $k \cdot p$ model. As we want the model to be most accurate near the Dirac cone energy ($E = 0$), we use w_b to weigh the central bands higher than the outer bands during the optimization procedure.

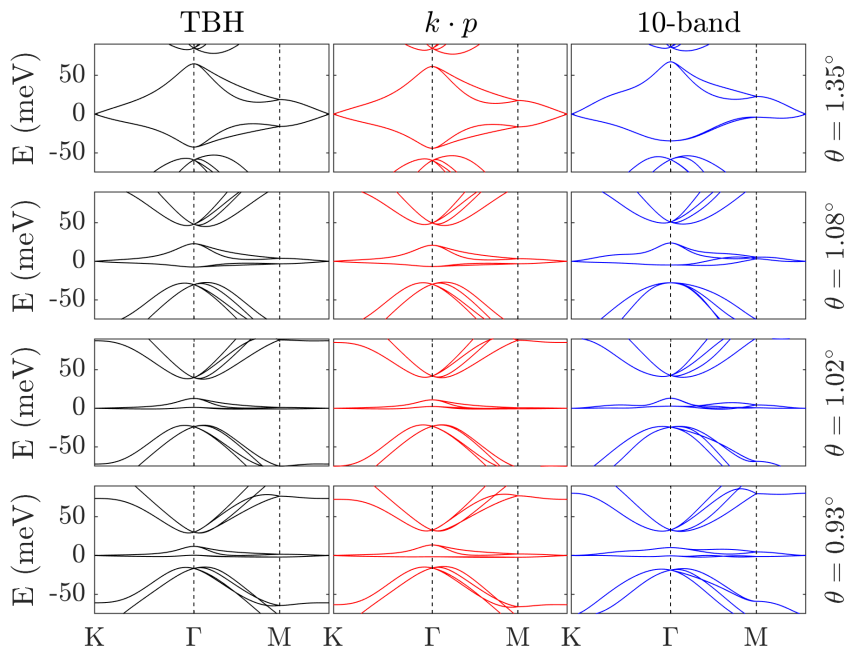


FIG. 1. Band structures for fully relaxed twisted bilayer graphene for a full tight-binding Hamiltonian, our *ab initio* $k \cdot p$ model, and a fitted 10-band model⁴. Four angles are checked, one well above the magic angle (1.35°), one slightly above (1.08°), one very close (1.02°) and one slightly below (0.93°).

IV. 10-BAND HAMILTONIAN

Following Ref. 4, we present the 10-band Hamiltonian. Our labeling of the 10 bands is connected to Ref. 4 in the following way: $AA_z \rightarrow p_z$, $AA_{\pm} \rightarrow p_{\pm}$, $DW \rightarrow \kappa$, and $AB/BA \rightarrow \eta$. The Hamiltonian is written in the momentum basis for simplicity, but each term represents a bond between two effective atomic orbitals in a realspace Hamiltonian. To simplify the notation, the following symbols are used to represent phases arising from bonds crossing the primitive unit-cell of the moiré cell or rotational symmetry constraints:

$$\phi_{lm} \equiv e^{-i\mathbf{k}\cdot(l\mathbf{a}_1+m\mathbf{a}_2)}, w \equiv e^{i2\pi/3}, \zeta \equiv e^{i2\pi/6}.$$

The 10-band Hamiltonian has diagonal blocks made of 4 orbital lattices: AA_z (1×1), AA_{\pm} (2×2), DW (3×3), and AB/BA (4×4). The off-diagonal blocks, labeled as C matrices, represent couplings between different orbital lattices.

$$H_{\mathbf{k}} = \begin{pmatrix} H_{AA_z} + \mu_{AA_z} & C_{AA_{\pm},AA_z}^{\dagger} & 0 & C_{AB/BA,AA_z}^{\dagger} \\ C_{AA_{\pm},AA_z}^{\dagger} & H_{AA_{\pm}} + \mu_{AA_{\pm}} & C_{DW,AA_{\pm}}^{\dagger} & C_{AB/BA,AA_{\pm}}^{\dagger} \\ 0 & C_{DW,AA_{\pm}} & H_{DW} + \mu_{DW} & C_{AB/BA,DW}^{\dagger} \\ C_{AB/BA,AA_z} & C_{AB/BA,AA_{\pm}} & C_{AB/BA,DW} & H_{AB/BA} \end{pmatrix}$$

Note that the term $C_{DW,AA_{\pm}}$ is set to zero here but in principle can be non-zero. the μ_i are multiples of the identity matrix which are the direct chemical potentials of the orbital lattices. However, due to the couplings present in each lattice the energy level of the isolated system in the flat-band manifold is slightly different (and called δ_i in the main text). The value of δ_i are given in Table I. The value of δ_{p_z} and δ_{κ} control the energies of the AA_z and DW portions of the flat bands at Γ , while δ_{\pm} controls the location of the Dirac cone touching point at K from AA_{\pm} ($p_x \pm ip_y$ type orbitals).

Param.	Orbital	Value
δ_{p_z}	AA_z	$\mu_{p_z} + 6t_{p_z}$
$\delta_{p_{\pm}}$	AA_{\pm}	$\mu_{p_{\pm}} - 3t_{p_{\pm}}$
δ_{κ}	DW	$\mu_{\kappa} + 4(t_{\kappa} + t'_{\kappa})$

TABLE I. Definition of three effective chemical potentials in the 10-band model⁴ and the geometric orbitals they are associated with.

We next tabulate the form of the orbital lattices on the diagonal blocks of the Hamil-

tonian. These generally depend on one parameter (t_i), or two parameters (t_i^\pm) where the \pm indexing is specifically chosen to allow for the breaking of time-reversal symmetry. The term t'_κ is primed to remind that it is a second nearest-neighbor bond, as having only first nearest-neighbor bonding on the Kagome lattice introduces a flat-band unrelated to the magic-angle phenomenon.

$$H_{AAz} = t_{p_z}(\phi_{01} + \phi_{11} + \phi_{10} + h.c.)$$

$$H_{AA\pm} = t_{p_\pm}(\phi_{01} + \phi_{11} + \phi_{10} + h.c.) \begin{pmatrix} 1 & 0 \\ 0 & 1 \end{pmatrix} + \begin{pmatrix} 0 & C_{p_\pm p_\pm}^\dagger \\ C_{p_\pm p_\pm} & 0 \end{pmatrix}$$

$$C_{p_\pm p_\pm} = t_{p_\pm p_\pm}^+(\phi_{01} + \phi_{\bar{1}\bar{1}}\omega + \phi_{10}\omega^*) + t_{p_\pm p_\pm}^-(\phi_{0\bar{1}} + \phi_{11}\omega + \phi_{\bar{1}0}\omega^*)$$

$$H_{DW} = t_\kappa \begin{pmatrix} 0 & \phi_{\bar{1}0} & 1 \\ 1 & 0 & \phi_{0\bar{1}} \\ \phi_{11} & 1 & 0 \end{pmatrix} + t'_\kappa \begin{pmatrix} 0 & \phi_{\bar{1}\bar{1}} & \phi_{\bar{1}0} \\ \phi_{0\bar{1}} & 0 & \phi_{10} \\ \phi_{01} & \phi_{11} & 0 \end{pmatrix} + h.c.$$

$$H_{AB/BA} = t_\eta \begin{pmatrix} 0 & e^{i\phi_\eta}(1 + \phi_{0\bar{1}} + \phi_{10}) \\ e^{-i\phi_\eta}(1 + \phi_{01} + \phi_{\bar{1}0}) & 0 \end{pmatrix} \otimes \mathbb{1}_{2 \times 2}$$

Finally, we tabulate the form of the inter-orbital hoppings. The formulae for $C_{AB/BA,i}$ depend on four real numbers (a, b, c, d) which represent how the AB/BA wave-function overlaps the AA and DW orbitals (see Ref. 4 for more details).

$$C_{AA\pm, AAz} = it_{p_\pm p_z}^+ \begin{pmatrix} \phi_{01} + \phi_{\bar{1}\bar{1}}\omega + \phi_{10}\omega^* \\ -(\phi_{0\bar{1}} + \phi_{11}\omega^* + \phi_{\bar{1}0}\omega) \end{pmatrix} - it_{p_\pm p_z}^- \begin{pmatrix} \phi_{0\bar{1}} + \phi_{11}\omega + \phi_{\bar{1}0}\omega^* \\ -(\phi_{01} + \phi_{\bar{1}\bar{1}}\omega^* + \phi_{10}\omega) \end{pmatrix}$$

$$C_{DW, AA\pm} = t_{\kappa p_\pm}^+ \begin{pmatrix} \phi_{\bar{1}0} & \phi_{\bar{1}\bar{1}} \\ \phi_{\bar{1}\bar{1}}\omega^* & \omega \\ \omega & \phi_{\bar{1}0}\omega^* \end{pmatrix} - t_{\kappa p_\pm}^- \begin{pmatrix} \phi_{\bar{1}\bar{1}} & \phi_{\bar{1}0} \\ \omega^* & \phi_{\bar{1}\bar{1}}\omega \\ \phi_{\bar{1}0}\omega & \omega^* \end{pmatrix}$$

$$\begin{aligned}
C_{AB/BA,AA_z} &= a \begin{pmatrix} -(\omega^* + \phi_{\bar{1}\bar{1}}\omega + \phi_{0\bar{1}})\zeta \\ (1 + \phi_{\bar{1}\bar{1}}\omega + \phi_{0\bar{1}}\omega^*)\zeta \\ (\omega^* + \phi_{\bar{1}0}\omega^* + \phi_{\bar{1}\bar{1}})\zeta^* \\ -(\omega^* + \phi_{\bar{1}0} + \phi_{\bar{1}\bar{1}}\omega)\zeta^* \end{pmatrix} \\
C_{AB/BA,AA_{\pm}} &= \begin{pmatrix} b(\omega + \phi_{\bar{1}\bar{1}}\omega^* + \phi_{0\bar{1}})\zeta^* & c(1 + \phi_{\bar{1}\bar{1}} + \phi_{0\bar{1}}) \\ c(1 + \phi_{\bar{1}\bar{1}} + \phi_{0\bar{1}}) & b(1 + \omega^*\phi_{\bar{1}\bar{1}} + \omega\phi_{0\bar{1}})\zeta^* \\ b(\omega + \phi_{\bar{1}0}\omega^* + \phi_{\bar{1}\bar{1}})\zeta & c(1 + \phi_{\bar{1}0} + \phi_{\bar{1}\bar{1}}) \\ c(1 + \phi_{\bar{1}0} + \phi_{\bar{1}\bar{1}}) & b(\omega + \phi_{\bar{1}0} + \phi_{\bar{1}\bar{1}}\omega^*)\zeta \end{pmatrix} \\
C_{AB/BA,DW} &= d \begin{pmatrix} i\phi_{10} & i\omega^* & i\phi_{0\bar{1}}\omega \\ i\phi_{10} & i\omega & i\phi_{0\bar{1}}\omega^* \\ -i & -i\omega^* & -i\omega \\ -i & -i\omega & -i\omega^* \end{pmatrix}
\end{aligned}$$

The 10-band Hamiltonian depends on 18 tunable parameters. We list them in Table II with a short description and the value obtained when fitted to a $\theta = 0.90^\circ$ $k \cdot p$ band-structure. In general, we find that this 10-band model with mostly nearest-neighbor coupling cannot perfectly recreate the *ab initio* $k \cdot p$ flat-bands in the magic-angle regime. It is likely that additional second or third nearest-neighbors are required to robustly recreate the dispersion of the flat-bands near the magic-angle. In future work we aim to generate these terms directly from a Wannierization of the $k \cdot p$ model.

V. PROJECTIONS OF THE 10-BAND MODEL

To obtain projections onto the 10-band model⁴, we begin with a trial wavefunction ϕ_0 with appropriate layer and sublattice symmetry. Next, we solve for n of the low-energy eigenvectors $\psi_{\mathbf{k}}^j$ of our $k \cdot p$ Hamiltonian $H_{\mathbf{k}}$, where \mathbf{k} spans a mesh sampling of the supercell Brillouin zone. Note that $\psi_{\mathbf{k}}^j$ is supported on a basis of *different* momenta, \mathbf{q} , which label the degrees of freedom of the $k \cdot p$ Hamiltonian, $H_{\mathbf{k}}$. We then compute the trial wavefunction's projection onto each $H_{\mathbf{k}}$, $\phi_{\mathbf{k}}^j = \sum_{\mathbf{q}} e^{i\mathbf{q}\cdot\mathbf{r}} |\psi_{\mathbf{k}}^j(\mathbf{q})\rangle \langle \psi_{\mathbf{k}}^j(\mathbf{q}) | \phi_0(\mathbf{r})$. Finally, we reconstruct the real space projection via $\phi(\mathbf{r}) = \int d\mathbf{k} \sum_{\mathbf{q}} e^{i\mathbf{q}\cdot\mathbf{r}} \phi_{\mathbf{k}}^j$, where \mathbf{q} are appropriate for $H_{\mathbf{k}}$.

In Fig. 1 of the main text, these projections are shown for a $k \cdot p$ model at $\theta = 0.90^\circ$.

Param.	Internal nnbr. of	Value
t_{p_z}	AA_z	-3.661
$t_{p_{\pm}}$	AA_{\pm}	-0.205
$t_{p_{\pm}p_{\pm}}^+$	AA_{\pm}	-2.260
$t_{p_{\pm}p_{\pm}}^-$	AA_{\pm}	-1.661
t_{κ}	DW	8.989
t'_{κ}	DW	-6.634
t_{η}	AB/BA	39.72

Param.	Inter Orbital nnbr. from	Value
$t_{p_{\pm}p_z}^+$	AA_{\pm} to AA_z	3.831
$t_{p_{\pm}p_z}^-$	AA_{\pm} to AA_z	1.149
$t_{\kappa p_{\pm}}^+$	DW to AA_{\pm}	-7.956
$t_{\kappa p_{\pm}}^-$	DW to AA_{\pm}	-5.678

Param.	Eff. Chem. Pot. of	Value
δ_{p_z}	AA_z	-12.10
$\delta_{p_{\pm}}$	AA_{\pm}	6.467
δ_{κ}	DW	5.933

Param.	Inter Orbital from AB/BA	Value
a	to AA_z	-24.69
b	to AA_{\pm}	-22.89
c	to AA_{\pm}	-10.51
d	to DW	36.67

TABLE II. 10-band model parameters and values for $\theta = 0.9^\circ$ given in meV.

Importantly, only one valley is considered in this projection, and we note that for a full physical tight-binding model, an additional 10 orbitals coming from the other monolayer valley must be included. With this in mind, we discuss the orbitals themselves. The AA orbitals are named after p -type orbitals, but that only describes their angular momenta: the orbitals themselves do not look like conventional p -orbitals on the moiré supercell. ψ_{AA_+} sits on a triangular lattice with most of its density on the B orbitals near the AA spot. To get ψ_{AA_-} one performs a mirror-plane symmetry bisecting the axis of rotation, putting the density onto the A orbitals near AA stacking. ψ_{AA_z} is also centered on the triangular lattice, but its density forms a three-lobed shape in each layer and sublattice index: it overlaps more strongly with the domain wall orbitals. ψ_{DW} sits on one third of a Kagome lattice, and the other 2 DW -like orbitals lie on the other 2 Kagome lattice sites (centers of the white lines in Fig. 1 of the main text). ψ_{AB} has a partner orbital also centered on the AB region, and can be thought of as a swapping of both the layer and sublattice index. That is to say, ψ_{AB} is primarily on sublattice A of layer 2, while its partner will be primarily on B of layer 1. There are also two orbitals centered on the BA region, with one primarily on sublattice A of layer 1 and the other on B of layer 2. This projection technique will be replaced by a proper Wannierization of the *ab initio* $k \cdot p$ model in the future, so we do not report numerical details of the projections.

VI. ON THE ACCURACY OF THE MODEL

Although the model is based on *ab initio* calculations, there may be shortcomings when comparing to experiment. For future comparison, we list some of the ways the magic-angle regime can be “shifted” in our model, due to varying assumptions placed on the $k \cdot p$ parameters. From DFT we obtain a graphene Fermi velocity of $v_F \approx 0.8 \times 10^6$ m/s, but changing the Fermi velocity proportionally changes the magic-angle. Increasing v_F by 10% will *decrease* the magic angle by 10%. Similarly, increasing the interlayer coupling by 10% will *increase* the magic-angle by 10% (this is the primary cause of the difference between the full and flat relaxed model). However, both v_F and the inter-layer coupling are directly proportional to “nearest-neighbor” tight-binding couplings (either intra-layer or inter-layer respectively). We expect that improving the DFT calculation, by e.g. including the GW approximation, would increase both v_F and the interlayer coupling, so it is not clear if such improvements would increase or decrease the magic-angle. The straining of the graphene layer shows up as a pseudo-gauge field for the monolayer Hamiltonians of our $k \cdot p$ model, moving the location of the Dirac cones in momentum space. Including this strain term generally *decreases* the magic-angle by 10%, moving the magic angle regime from 1.1° in the unrelaxed model to 1.0° in the fully relaxed model, consistent with previous tight-binding modeling⁵. It is also possible that the bilayer’s energy can be further optimized by allowing for shearing between the layers, and this may move the magic-angle regime by up to 5%⁶.

¹ S. Zhou, J. Han, S. Dai, J. Sun, and D. J. Srolovitz, [Phys. Rev. B **92**, 155438 \(2015\)](#).

² S. Carr, D. Massatt, S. B. Torrisi, P. Cazeaux, M. Luskin, and E. Kaxiras, [arXiv:1805.06972 \[cond-mat.mes-hall\] \(2018\)](#).

³ R. Bistritzer and A. H. MacDonald, [Proceedings of the National Academy of Sciences of the United States of America **108**, 12233 \(2011\)](#).

⁴ H. C. Po, L. Zou, T. Senthil, and A. Vishwanath, [arXiv:1808.02482 \[cond-mat.str-el\] \(2018\)](#).

⁵ N. N. T. Nam and M. Koshino, [Phys. Rev. B **96**, 075311 \(2017\)](#).

⁶ X. Lin, D. Liu, and D. Tomnek, [arXiv:1811.00413 \[cond-mat.mes-hall\] \(2018\)](#).